Journal of Catalysis **196,** 134–148 (2000)
doi:10.1006/jcat.2000.3016, available online at http://www.idealibrary.com on IDEAL®

The Use of Nuclear Magnetic Resonance, Microcalorimetry, and Atomic Force Microscopy to Study the Aging and Regeneration of Fluid Cracking Catalysts

M. L. Occelli,* M. Kalwei,† A. Wölker,† H. Eckert,† A. Auroux,‡ and S. A. C. Gould§

*MLO Consulting, 6105 Black Water Trail, Atlanta, Georgia 30328; †Institut für Physikalische Chemie, Westfälische Wilhelms Universität Münster, Schlossplatz 7, D 48149, Münster, Germany; ‡Institut de Recherches sur la Catalyse, CNRS, 2 Avenue A. Einstein, 69626 Villeurbanne, France; and §W. M. Keck Science Center, The Claremont Colleges, Claremont, California 91711

Received April 24, 2000; revised July 27, 2000; accepted July 31, 2000

The accelerated steam-aging procedure (with 100% steam at 760°C for 5 h) used in this study reduces the surface area (SA) of a fresh fluid cracking catalyst (FCC) to a value close to that measured in the corresponding equilibrium sample. In addition, ^{29}Si nuclear magnetic resonance (NMR) spectra of steam-aged and equilibrium FCC samples are practically indistinguishable. However, the steam-aged and equilibrium FCCs have different pore structures, initial heats of ammonia and pyridine chemisorption as well as different distributions of Al(IV), Al(V), and Al(VI) species. The ^{29}Si NMR spectrum of the fresh or steam-aged FCC can be considered a superposition of the spectra of its components (the HY zeolite, kaolin, and aluminosilicate matrix). After aging, the ^{29}Si NMR spectrum of zeolitic component is reduced to one main dominant resonance near the −107 ppm representative of T(4Si, 0Al) sites. Thus extensive dealumination of the cracking component in FCCs occurs during recirculation in a fluid cracking catalyst unit (FCCU). Similar conclusions have been obtained from ^{27}Al magic angle spinning (MAS) NMR spectra. Microcalorimetry experiments with ammonia and pyridine have shown that after aging either under microactivity test (MAT) conditions or in a FCCU, the fresh FCC undergoes severe losses in acid site density while retaining most of the strength of its strongest Lewis acid sites. These sites, and the retention of an open micro- and mesoporosity, are believed to be responsible for the aged FCCs' cracking activity. Atomic force microscopy images have shown that the equilibrium FCC contains on its surface debris attributed to nickel and vanadium oxides and that most of this debris disappears from the surface of the regenerated catalyst. ^{27}Al and ^{29}Si MAS NMR spectroscopy results have revealed that the demetallation (DEMET) process, in addition to removing most of the metal contaminants, leaves a completely dealuminated zeolitic component. These results indicate that cracking activity in these FCCs does not depend on the presence of framework Al in the faujasite crystals present. The increase in acidity and microporosity is consistent with the observed enhanced cracking activity, under MAT conditions, of the regenerated FCC.

INTRODUCTION

Catalyst production for the transformation of crudes into gasoline and other fuel products is a $2.1 billion/year business and fluid cracking catalysts (FCCs) represent almost half of the refinery catalyst market (1). About 1100 tons/day of FCCs are used worldwide in over 200 fluid cracking catalyst units (FCCUs) (2). During the cracking reactions, the FCC surface is contaminated by metals (Ni, V, Fe, Cu, Na) and by coke deposition. As a result, the catalyst activity and product selectivity are reduced to unacceptable levels, thus forcing refiners to replace part of the recirculating equilibrium FCC inventory with fresh FCC to compensate for losses in catalyst performance (3). The spent FCC can be disposed of in landfills, used in cement kilns, or used as a source of metals or, alternatively, it can be regenerated for reuse. FCC regeneration has met some success. In fact, over 13,630 metric tons of spent FCC have been recovered and recycled in a single FCCU of a major U.S. refinery (2).

The demetallation (DEMET) process (4) for the regeneration of spent FCC consists of a demetallization procedure involving a sequence of pyrometallurgical (calcining, sulfiding, chlorinating, and nitrogen stripping) and hydrometallurgical (acid-leaching, washing, drying) steps aimed at removing metal contaminants from the spent catalyst (2). It is the purpose of this paper to investigate the physicochemical changes that a FCC undergoes during accelerated aging (steam-aging) in a laboratory, during use in a refinery FCCU, and after regeneration of the spent FCC with the DEMET process.

FCCs have been studied with a broad range of microscopic techniques that include transmission electron microscopy (TEM), scanning electron microscopy (SEM) (5–9), and high-resolution electron microscopy (HREM) (10). TEM, SEM, and HREM images have revealed the presence of metal contaminants, metal agglomeration, and metal diffusion as well as crystallite fracture with mesopore formation in the zeolite contained in FCCs (9, 10). Information concerning the size, shape, and architecture of the surface requires imaging techniques with greater spatial resolution such as STM (11) or atomic force microscopy (AFM) (12, 13). In fact, AFM images can represent FCC

0021-9517/00 $35.00

surfaces with molecular-scale resolution and can distinguish between the FCC main components (14).

In this paper the surface topography of FCCs will be studied with an atomic force microscope operating in a contact or tapping mode. Changes in the FCC acidic component (an HY-type zeolite) and changes in FCC acidity will be investigated using magic angle spinning (MAS) nuclear magnetic resonance (NMR) and microcalorimetry experiments at 150°C with ammonia and pyridine as the probe molecules.

EXPERIMENTAL

Nitrogen Porosimetry

Nitrogen sorption isotherms at liquid nitrogen temperature were obtained with a Micromeritics ASAP 2010 unit using a volumetric technique. Prior to analysis, samples were outgassed *in vacuo* at 400°C for at least 10 h. A precise description of the micropore system was obtained by sending successive increments of analysis gas (usually doses of 2 cc/g of sample) and waiting for thermal equilibration. BET surface areas (15) were calculated from nitrogen uptakes at relative pressures ranging from 0.05 to 0.30. The total pore volume was derived from the amount of nitrogen adsorbed at a relative pressure close to unity (in practice $p/P_0 = 0.995$) by assuming that all the accessible pores had been filled with condensed nitrogen in the normal liquid state.

Pore size distribution was calculated from density functional theory methods using the adsorption branch of the isotherm and assuming slit-like pores (16–19). Although the density functional theory has been developed for adsorption on microporous carbons, it can also be used to determine the pore size distribution of silicas, aluminosilicates, and aluminas (20).

Solid State NMR

^{29}Si NMR spectra were recorded at 59.6 MHz on a modified Bruker CXP300 spectrometer. Samples were spun in cylindrical 7-mm zirconia rotors at spinning speeds near 4 kHz; 90° pulses of 6 μs in length and 30-s recycle delays were used in all cases. Chemical shifts were determined relative to tetramethylsilane as an external reference. ^{27}Al MAS NMR spectra were obtained at 130.2 MHz, using a Bruker Avance (DSX) 500 spectrometer. Samples were spun in cylindrical 4-mm zirconia rotors at a spinning frequency of 12 kHz. The spectra were recorded with short pulses of 2 μs (flip angle $<45°$) and relaxation delays of 1 s. Resonance shifts are reported using liquid samples of 1 M aqueous solutions of $Al(NO_3)_3$ as external reference standard. Because the exact spectral parameters of the Al(IV), Al(V), and Al(VI) signal components are not known (due to a distribution of quadrupolar coupling parameters), no ^{27}Al lineshape deconvolution was attempted.

Microcalorimetry

Heat of adsorption of NH_3 and pyridine was measured using a heat-flow microcalorimeter of the Tian-Calvet type (from Setaram) linked to a glass volumetric line. Successive doses of gas were sent onto the sample until a final equilibrium pressure of 133 Pa was obtained. The equilibrium pressure relative to each adsorbed amount was measured by means of a differential pressure gauge from Datametrics. The adsorption temperature was maintained at 150°C. Primary and secondary isotherms were collected at these temperatures. All samples were dried overnight under vacuum at 400°C before calorimetric measurements were taken.

Atomic Force Microscopy

The FCC microspheres were glued onto a steel disk with epoxy resin. After the glue dried, the AFM tip was carefully guided to the middle of the particle, thus beginning the imaging session. The AFM used in this work was a Nanoscope III instrument (from Digital Instruments, Santa Barbara, CA) operating in contact mode or tapping mode; the AFM was calibrated using mica. The images presented in this paper contain either 256×256 or 512×512 data points and were obtained within a few seconds. The Si_3N_4 cantilever (with integral tip) had a length in the range 60 to 120 μm with spring constants in the range 0.1 to 0.6 N/m. Typical forces applied to obtain these images ranged from 1.0 to 100 nN. Several hundred images were examined using different cantilevers. The cross-sectional analyses on these images were always along, or nearly along, the fast scan direction in order to further reduce the effects of drift. In order to avoid tip-related artifacts, imaging was performed with minimal (less than 10 nN) force, and image features were reproduced before being accepted as representative. Moreover, by rotating the image, by changing scan speeds, scan times, and imaging forces, and by acquiring images invariant with time, it is believed that artifacts can be identified and separated from real features when studying the surfaces of FCC with an AFM operating in contact mode.

Microactivity Testing (MAT)

Microactivity testing (MAT) was conducted with a Kuwait VGO and a reactor temperature of 540°C, using a 60-s injection time and a cat/oil (C/O) ratio of 3.0. Gas oil inspection is given in Table 1. Prior to microactivity evaluation, the fresh FCC microspheres were steam-aged for 5 h with 100% steam at ~760°C and 1 atm. The fresh FCC, together with an equilibrium FCC from a major U.S. refinery and a spent FCC regenerated by the DEMET process (2, 4), was obtained from Coastal.

TABLE 1

Kuwait Vacuum Gas Oil Inspection

°API gravity	20.2
Specific gravity	0.9330
Total nitrogen (wppm)	1027.0
Basic nitrogen (wppm)	301.0
Total sulfur (wt%)	3.1
Aniline point (°C)	78.2
Conradson carbon (wt%)	0.24
Refractive index	1.5184
Nickel (wppm)	0.18
Vanadium (wppm)	0.16

TABLE 2

Elemental Analyses (wt%) for a Commercial FCC Sample before Use, after Use in a FCCU, and after Regeneration

	Fresh FCC	Equil. FCC	Regen. FCC
SiO_2	66.0	57.0	58.6
Al_2O_3	30.9	38.1	38.5
SiO_2/Al_2O_3	3.6	2.5	2.6
Re_2O_3	1.6	1.8	1.2
Na_2O	0.47	0.57	0.46
NiO	0.03	0.60	0.03
V_2O_5	—	0.99	0.19
Fe_2O_3	0.79	0.85	0.19
TiO_2	0.89	1.37	0.55

Note. Re_2O_3 is the sum of the rare earth present, expressed in the form of oxides. Values <0.001 wt% have not been reported.

RESULTS AND DISCUSSION

XRD and Porosimetry Results

Powder XRD results in Fig. 1 indicate that after steam-aging, the crystallinity of the fresh, commercially available FCC is somewhat greater than that of its equilibrium counterpart and more closely resembles that observed in the regenerated spent FCC; see Figs. 1A–1C. These differences have been attributed to the presence of metal contaminants on the equilibrium FCC surface. Elemental analysis data for the three FCCs under study are listed in Table 2.

The commercial FCC contains, as a cracking component, an HY-type zeolite stabilized by low levels of rare earth cations. Iron (mostly Fe_2O_3) and titania (mainly rutile) are impurities associated with the clay (kaolin) used during the manufacturing process. In addition to metal (Ni and V) deposition, the equilibrium FCC undergoes a decrease in its SiO_2/Al_2O_3 molar ratio from 3.6 to 2.5, probably because of silica losses (21) during the thermal and hydrothermal treatments experienced during the regeneration cycle of the FCCU from which it was obtained; see Table 2. That is, during aging in a FCCU, the extraframework silica generated as a result of zeolite (21), matrix, and clay degradation hydrolyzes to form volatile Si compounds, such as $Si(OH)_4$, that are lost in the regenerator. The demetallation procedure used leaves the bulk SiO_2/Al_2O_3 molar ratio of the catalyst almost unchanged while drastically reducing its metal (Ni, V, Fe) content; see Table 2.

The FCC under study can be considered an agglomeration of kaolin platelets and faujasite crystals held together by an aluminosilicate matrix. Representative nitrogen sorption isotherms for these catalysts are presented in Fig. 2.

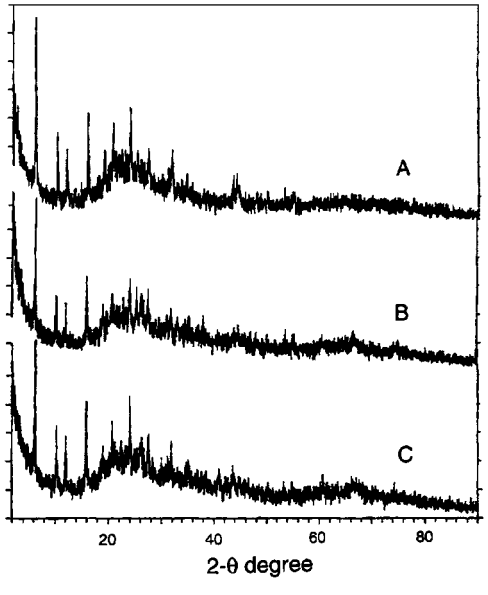

FIG. 1. Powder X-ray diffractograms of (A) the steam-aged fresh FCC, (B) the equilibrium FCC, and (C) the regenerated FCC.

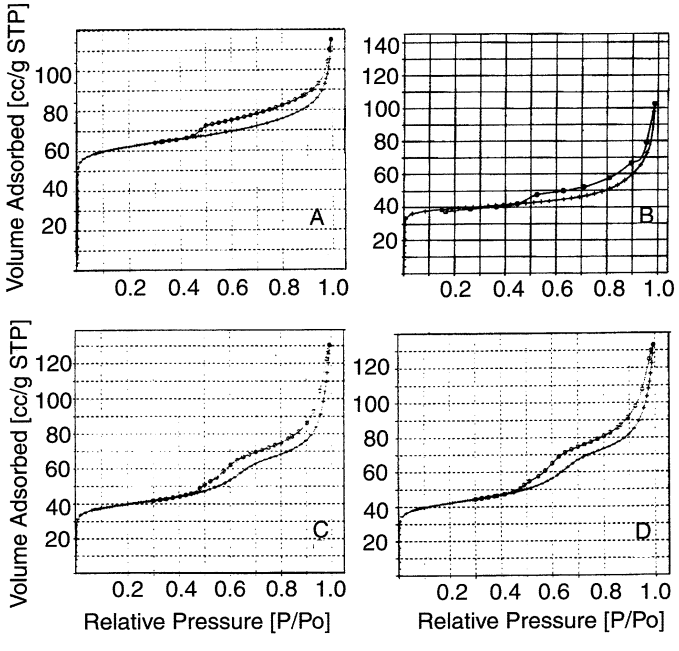

FIG. 2. Nitrogen sorption isotherms for (A) fresh FCC, (B) steam-aged FCC, (C) equilibrium FCC, and (D) regenerated FCC.

For $p/P_0 < 0.2$, nitrogen adsorption on the fresh FCC is represented by a type I isotherm (22) typical of microporous materials such as zeolites; see Fig. 2A. At $p/P_0 = 0.2$, most of the accessible micropores are filled with adsorbate. However, at $p/P_0 > 0.2$ the isotherms slowly increase with p/P_0 values, suggesting the deposition of additional sorbate in the intraparticle voids that exist between the FCC components. Near $p/P_0 = 0.7$ the adsorption isotherm rises abruptly due to capillary condensation in meso- and macropores.

After steam-aging there is a decrease in surface area (SA) and a loss in sorption capacity but the shape of the sorption isotherm remains unchanged; see Fig. 2B. In contrast, for the equilibrium or regenerated FCC, isotherms become type IV, indicating the presence of mesopores (22); see Figs. 2C and 2D. Three well-defined stages may be identified in these isotherms. Initially, there is a fast increase in nitrogen uptake at low relative pressures, corresponding to monolayer–multilayer adsorption on the micropore walls. Then at intermediate relative pressures, there is a step indicative of capillary condensation within mesopores. In this case, the inclination of the step indicates that these mesopores have a wide range of sizes and shapes. Finally as the pressure approaches saturation, $(p/P_0) \rightarrow 1$, there is a sharp rise in N_2 uptake. In Fig. 2, the small hysteresis loops are typical of meso- and macroporous materials and are indicative of the difference between condensation and evaporation of the probe molecule within the pores of the FCCs examined.

Variations in incremental pore volumes with pore width are shown in Fig. 3; nitrogen porosimetry results are in Table 3. The fresh FCC under study is mainly a microporous material with 94% of its total SA, and 47% of its total pore volume (PV), in pores with $d \leq 2.0$ nm. The pore size distribution in Fig. 3A further illustrates that the fresh FCC is essentially a microporous solid with an average pore diameter (APD) near 0.85 nm. The microporous nature of these microspheres results mainly from the presence of HY-type crystals and, to a lesser extent, from the aluminosilicate matrix (20). The porous structure of a FCC strongly depends on its composition and method of preparation and it is not uncommon to find fresh catalysts with bimodal distribution of pore sizes that include micro- as well as mesopores (23).

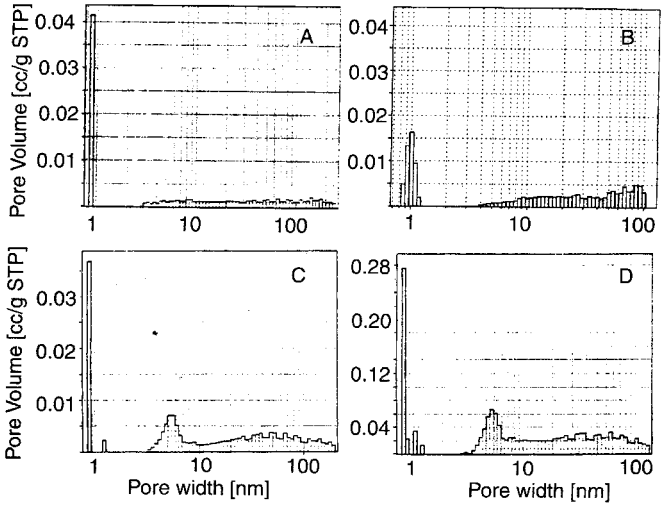

FIG. 3. The dependence of incremental pore volume on pore width for (A) fresh FCC, (B) steam-aged FCC, (C) equilibrium FCC, and (D) regenerated FCC.

TABLE 3

Same Surface Area (SA) and Pore Volume (PV), from Nitrogen Porosimetry Data, Using Different Methods

FCC	SA (m^2/g)			Micro. SA	PV (cc/g)	
	Lang.	BET	DFT	Meso. SA	BET	DFT
Fresh	285	194	182	17.1	0.18	0.16
Steamed	182	125	103	9.3	0.16	0.14
Equilibrium	189	127	107	3.8	0.20	0.18
Regenerated	200	136	103	3.8	0.20	0.16

Note. The FCC samples were degassed under vacuum at 400°C for 10 h.

After aging under MAT conditions (or in a FCCU), the catalyst loses part of its SA and crystallinity and with it some of its SA and PV; see Table 3. Whereas in the fresh FCC all micropores have a pore width near 0.85 nm, in the steam-aged FCC there is a distribution of micropores with pore width in the range 0.85–1.2 nm; see Fig. 3B. In addition, the microspheres' meso- and macroporosity increases; only 32% of the total pore volume in the steam-aged FCC is found in micropores. As a result, the ratio of the SA in micro- and mesopores decreases from 17.1 in the fresh FCC to 9.3; see Table 3.

The equilibrium FCC retains its single set of micropores while forming new mesopores with an APD of 5.5 nm; see Fig. 3C. In the equilibrium FCC, 77% of the catalyst SA and 22% of its PV are in micropores. The appearance of new micro- and mesopores is probably the result of HY crystal degradation and fracture, as seen by HREM (9, 10), and, to a lesser extent, the result of changes in the kaolin and aluminosilicate matrix structure; see Fig. 3C. The ratio of the SA in micro- and mesopores decreases from 17.1 in the fresh FCC to 3.8, further illustrating the different pore structures that exist in these steam-aged and equilibrium FCCs; see Table 3.

After regeneration, the distribution of pores in the range 5 to 100 nm remains practically unchanged; see Figs. 3C and 3D. The minor increase in microporosity seen in Fig. 3D is attributed to metal (Ni, V, Fe) removal from the regenerated FCC microspheres. Metal oxides such as vanadia can fill and block the FCC small micropores. Removal of vanadia and other metal oxides exposes these micropores to nitrogen sorption and gas oil cracking. Thus it appears that aging decreases the FCC microporosity and increases

pores in the small (<10 nm) mesopore range. The demetallation process used to regenerate this type of FCC removes pore-blocking metal oxides without significantly altering the equilibrium catalyst pore structure; see Tables 2 and 3 and Figs. 3C and 3D.

^{29}Si NMR Results

In a typical preparation, FCCs are synthesized by adding to an aluminosilicate slurry a clay (usually kaolin) together with the desired amount of an HY-type zeolite to obtain materials with the desired cracking and physical properties. The resulting mixture is then spray-dried to form microspheres 80–140 μm in diameter that, after washing, drying, and calcination, are sent to refiners.

^{29}Si NMR spectra for the aforementioned FCC components are shown in Fig. 4. The spectrum for the reference HY in Fig. 4A is similar to that published elsewhere (24). The spectrum in Fig. 4B for the steam-aged (100% steam at 760°C) HY reveals an extensive dealumination of the faujasite structure and has already been described in the literature (24). Equally noteworthy are the transformations that have occurred in the gel and kaolin (the matrix components) after thermal treatments. Structurally, kaolin is a clay mineral with the formula $Si_2\ Al_2O_5(OH)_4$, consisting of a layer of silicon atoms in tetrahedral coordination joined to a sheet of aluminum atoms in octahedral coordination having two-thirds cation site occupancy (25). As a result, its ^{29}Si spectrum contains a single sharp resonance at −91.5 ppm representing T(3Si, 1Al) sites; see Fig. 4C and Table 4. The structural transformation suffered by kaolin during calcination is illustrated by the very broad asymmetric ^{29}Si spectrum in Fig. 4D with a peak maximum near −108 ppm. After steam-aging at 760°C, the kaolin sample displays a considerably broadened spectrum that is even more asymmetric; see Fig. 4E. The spectra in Figs. 4D and 4E can be decomposed into two components. In Table 4 the high-frequency resonance is attributed to silica generated during thermal losses of hydroxyl groups and decomposition of the kaolin structure while the low-frequency resonance is attributed to distorted T(3Si, 1Al) sites in the amorphous aluminosilicate residue.

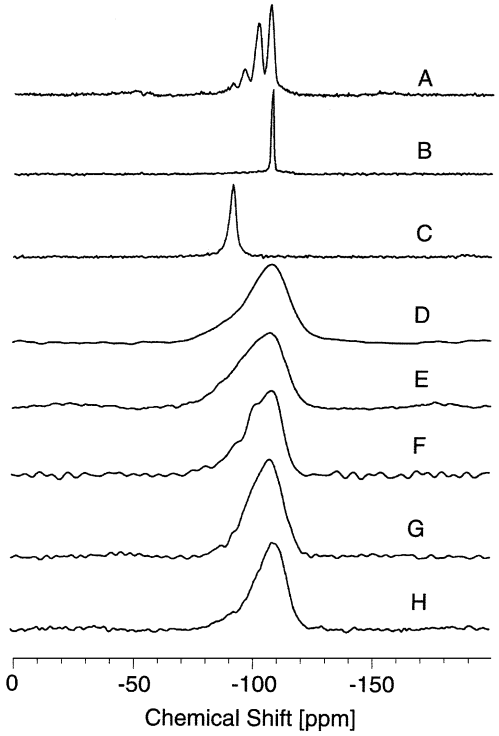

FIG. 4. ^{29}Si MAS NMR spectra of (A) HY (LZY-82), (B) steam-aged HY, (C) air-dried kaolin, (D) kaolin calcined at 600°C/1 h, (E) steam-aged kaolin, (F) air-dried AAA-alumina, (G) AAA-alumina calcined at 600°C for 1 h, and (H) steam-aged AAA-alumina.

TABLE 4

^{29}Si Chemical Shifts (-ppm) for Kaolin and AAA-Gel, the FCC Matrix Components, after Thermal and Hydrothermal Treatments (% Relative Intensities Are in Parentheses)

	Chemical shifts (-ppm)			
Kaolin-400	91.5 (100)	—	—	—
Kaolin-600	92.6 (36.0)	—	—	108.5 (64.0)
Kaolin-steamed	93.8 (39.0)	—	—	108.0 (61.0)
AAA-Gel-400	92.9 (11.1)	—	100.6 (28.2)	108.0 (60.7)
AAA-Gel-600	—	96.3 (22.1)	—	107.5 (77.9)
AAA-Gel-steamed	—	94.8 (21.3)	—	109.6 (78.7)

AAA-alumina is an aluminosilicate gel prepared from the reaction of sodium silicate (such as N-silicate from the PQ Corp.) and a soluble source of aluminum (such as sodium aluminate or $Al_2(SO_4)_3$). After drying at 400°C, the ^{29}Si spectrum of this gel contains resonances near −92.9, −100.6, and −108.0 ppm; see Fig. 4F. Most likely these components arise from different T(nSi, (4-n)Al) sites, although in addition T(3Si, 1OH) and T(2Si, 2OH) environments with one or two silanol groups may contribute to the signal. In contrast, the ^{29}Si spectrum of the AAA-alumina sample calcined at 600°C can be deconvoluted into only two components (at −107.5 and −96.3 ppm), indicating that these thermal and hydrothermal treatments have modified the aluminosilicate structure; see Fig. 4G. After steam-aging, the shape of the spectrum remains the same but chemical shift values change; see Fig. 4H.

Spectra and chemical shifts for the four FCC samples under study are summarized in Fig. 5 and in Table 5, respectively. Figure 5A represents the ^{29}Si NMR spectrum of the fresh FCC. Deconvolution of the entire lineshape indicates that the signal pattern arises from the overlap of the kaolin signal near −91.0 ppm and from four additional sharp resonances at −110.0, −106.6, −101.3, and −95.3 ppm; see Fig. 5A. The upfield resonance at −110.0 ppm most likely

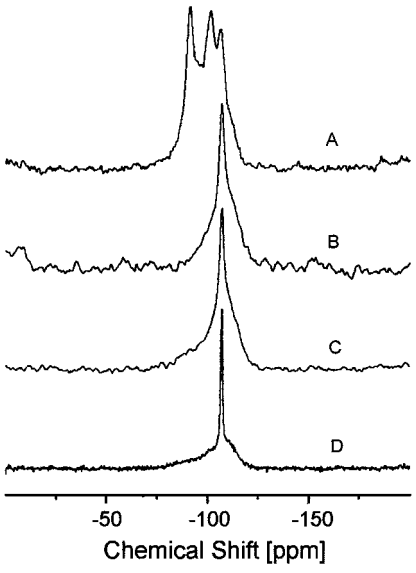

FIG. 5. ^{29}Si MAS NMR spectra of (A) fresh FCC, (B) steam-aged FCC, (C) equilibrium FCC, and (D) regenerated FCC.

arises from amorphous extraframework silica (26). Resonances at −106.6, −101.3, and −95.3 ppm are attributed to the T(4Si, 0Al), T(3Si, 1Al), and T(2Si, 2Al) sites of the RE-stabilized HY-type zeolite used as the FCC cracking component; see Table 5 and Fig. 5A. The additional signal intensity visible at −86.0 ppm and that upfield of the −110.0 ppm peak are attributed to T(2Si, 2OH) sites and to the presence of amorphous silica in the FCC matrix, respectively. Comparison of Fig. 5A with the spectra in Fig. 4 shows that the ^{29}Si spectrum of the fresh FCC can be viewed as a superposition of the spectra of its three fresh components; see Figs. 4A, 4C, and 4F.

TABLE 5

^{29}Si NMR Chemical Shifts (CS, -ppm) and Relative Intensities (Area%) for the Four FCC Samples Under Study

CS	Area%	Assignment
	Fresh FCC	
86.1	14.0	T(2Si, 2OH) (matrix)
91.0	18.6	Kaolin
95.3	13.2	T(2Si, 2Al) (zeolite)
101.3	29.5	T(3Si, 1Al) (zeolite)
106.6	14.0	T(4Si, 0Al) (zeolite)
110.0	5.4	Silica (matrix)
113.1	5.3	Silica (matrix)
	Equilibrium FCC	
90.2	14.9	T(2Si, 2Al) (matrix)
102.8	16.7	T(3Si, 1Al) (matrix)
107.0	14.5	T(4Si, 0Al) (zeolite)
109.9	52.1	T(4Si, 0Al) (matrix)
	Steamed FCC	
90.2	10.6	T(2Si, 2Al) (matrix)
95.7	3.2	T(2Si, 2Al) (zeolite)
102.8	21.0	T(3Si, 1Al) (matrix)
107.0	1.5	T(4Si, 0Al) (zeolite)
109.8	53.6	T(4Si, 0Al) (matrix)
	Regenerated FCC	
90.2	17.2	T(2Si, 2Al) (matrix)
101.2	16.8	T(3Si, 1Al) (matrix)
107.0	23.5	T(4Si, 0Al) (zeolite)
109.9	42.4	T(4Si, 0Al) (matrix)

In the ^{29}Si spectrum of the steam-aged and equilibrium FCCs, the typical peak pattern attributed to the HY-type zeolite used as cracking component, disappears and is replaced by an intense signal at −107.0 ppm representing a zeolitic T(4Si, 0Al) resonance; see Figs. 5B and 5C. The spectra in these figures are practically indistinguishible, suggesting that steam-aging under MAT conditions or aging in a FCCU produces similar silicon environments. Comparison with Fig. 5A reveals that the zeolite has undergone extensive dealumination under both conditions. The relatively sharp zeolitic resonance seen in Figs. 5B and 5C is superimposed upon a broad complex background, revealing the siliceous products generated by the transformation of the zeolitic, kaolin, and AAA-gel components under these aging conditions. On the whole, as already observed for the fresh FCC, the ^{29}Si spectrum of the steam-aged sample can again be viewed as a superposition of the spectra of its three steam-aged components; see Figs. 4B, 4E, and 4H. However, owing to the multitude of chemical environments present, a quantitative lineshape deconvolution in terms of these individual components was not attempted. Nevertheless, a simpler deconvolution of the broad background into three broad resonances near −110 (±1) ppm, −102 (±1) ppm, and −90 (±1) ppm provided acceptable fits. These chemical shifts are assignable to T(4Si, 0Al), T(3Si, 1Al), and T(2Si, 2Al) sites in the amorphous environment produced during the aforementioned transformation of the matrix components. Furthermore, we cannot exclude the possibility that residual T(3Si, 1OH) and T(2Si, 2OH) sites make spectral contributions to the resonances observed near −102 and −90 ppm, respectively. Figure 5D shows the ^{29}Si spectrum of the regenerated FCC. Compared to the spectrum of its equilibrium counterpart, the width of the −107.1 ppm peak is greatly reduced, indicating a higher degree of local order in the zeolitic component. This finding is corroborated by the comparison of the corresponding X-ray powder diffraction linewidths (not shown). Furthermore, the fractional area attributed to this resonance is noticeably larger than in the equilibrium FCC sample; see Table 5. No evidence remains for other silicon sites of zeolitic origin. Thus, the regeneration process leaves a cracking component without recognizable framework Al and containing only T(4Si, 0Al) sites. As with the steam-aged and the equilibrium FCCs, a complex broad background is observable, which can be deconvoluted into three broad resonances whose assignment has been discussed above.

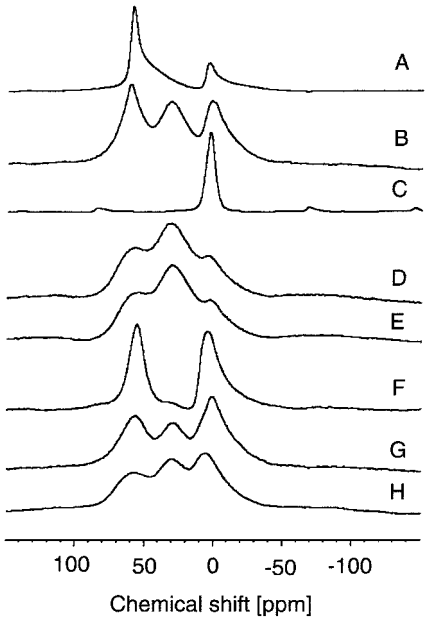

FIG. 6. ^{27}Al MAS NMR spectra of (A) HY (LZY-82), (B) steam-aged HY, (C) air-dried kaolin, (D) kaolin calcined at 600°C for 1 h, (E) steam-aged kaolin, (F) air-dried AAA-alumina, (G) AAA-alumina calcined at 600°C for 1 h, and (H) steam-aged AAA-alumina.

^{27}Al NMR Results

The ^{27}Al NMR spectra of the FCC components are shown in Fig. 6. As expected, the spectrum of the calcined HY (LZY-82) contains resonances near 0 and 60 ppm representing Al(VI) and Al(IV) species, respectively; see Fig. 6A. The resonance at 60 ppm overlaps another centered near 30 ppm attributed to Al(V) (27) species or to highly distorted Al(IV) (28). After steam-aging there is some lattice degradation and the relative intensity of the resonance near 60 ppm decreases owing to the conversion of Al(IV) to extraframework Al(V) and (VI) species; see Fig. 6B. Recent results obtained using a double-rotation spinning technique (29, 30) for the study of Al in zeolites have led to the conclusion that extraframework Al contains, in addition to Al(V) and Al(VI), some Al(IV) species. By comparing Al MAS NMR with Al CP MAS NMR, it has been shown that in steam-aged HY a substantial portion of the resonance attributed to Al(IV) results from the presence of extraframework Al species (31).

As anticipated, only Al(VI) is observed in the spectrum in Fig. 6C for kaolin. On calcination at 600°C, XRD data (not shown) indicate that the kaolin structure collapses, leaving an X-ray amorphous aluminosilicate residue referred to as metakaolin (25). The ^{27}Al spectrum in Fig. 6D indicates that this amorphous residue consists of a network of Al(IV), Al(V), and Al(VI) species that is not greatly affected by steaming; see Fig. 6E.

After drying at 400°C in air, the AAA-alumina spectrum contains only two main resonances resulting from tetrahedrally and octahedrally coordinated Al species (20); see Fig. 6F. However, after the gel was calcined at 600°C in air, the ^{27}Al spectrum reveals that significant conversion of tetrahedral Al to five and six coordinated Al species has occurred; see Fig. 6G. Losses of Al(IV) sites and the formation of additional Al(V) species increase after steam-aging; see Fig. 6H.

The corresponding ^{27}Al spectra of the four FCCs are shown and compared in Fig. 7. The spectrum of the fresh FCC in Fig. 7A is dominated by an intense and sharp peak at 3.7 ppm arising mainly from the octahedral Al in the clay and, to a lesser extent, from Al(VI) species in the zeolite and in the matrix; see Figs. 6A, 6C, and 6F. Moreover, a resonance shift near 59.0 ppm signifies the presence of tetrahedrally coordinated Al resulting mainly from the FCC zeolitic cracking component. As indicated by the low-frequency shoulder, this peak may also contains a contribution from Al(IV) species in the aluminosilicate matrix (20).

In the steam-aged microspheres, there is a significant conversion of Al(VI) to Al(V) and Al(IV) due to transformations in the FCC matrix; see Fig. 7B. As a result, the Al(IV), Al(V), and Al(VI) species present seem to make contributions of comparable magnitude to the total signal intensity. The ^{27}Al spectrum of the steam-aged FCC in Fig. 7B is well understood in term of the spectra of its steam-aged components; see Figs. 6B, 6E, and 6H.

In the equilibrium FCC (and in the regenerated FCC), ^{27}Al NMR spectra are dominated by the Al(VI) resonance

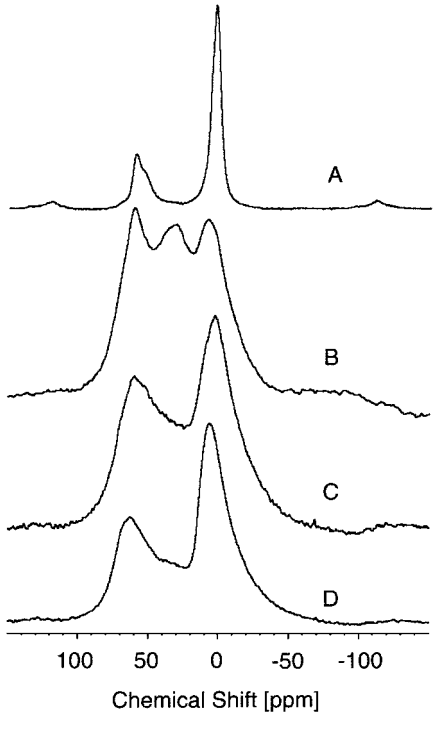

FIG. 7. ^{27}Al MAS NMR spectra of (A) fresh FCC, (B) steam-aged FCC, (C) equilibrium FCC, and (D) regenerated FCC.

and only minor amounts of Al(V) can be observed; see Figs. 7C and 7D. Since in the corresponding ^{29}Si spectrum the T(4Si, 0Al) resonance is the only one observable for the FCC zeolitic component, the Al(IV) observed in Figs. 7B–7D represents mainly extraframework Al(IV) species.

Traditionally, kaolin has been considered an inert component that provides the desired density and attrition resistance to FCCs. NMR results in Figs. 6 and 7 have shown that this clay (and to a lesser extent the AAA-gel in the matrix) is a source of Al(V) species that if available could affect gas oil cracking. Moreover, the different distribution of Al species in steam-aged and equilibrium FCCs shown in Figs. 7B and 7C could contribute to the different cracking properties exhibited by these two FCCs under MAT conditions.

Microcalorimetry Results

Heat flow microcalorimetry with pyridine as the probe molecule has already been used to study the effects that steam-aging times have on FCCs prepared from the hydrothermal transformation of calcined kaolin microspheres in alkaline solutions (32). The strength of the main population of sites in these clay-based FCCs was observed to decrease with increasing steam-aging times and after only 15 min of steam-aging with 100% steam at 787°C (and 1 atm) they lost most of their total acidity (32).

Although microcalorimetry cannot distinguish betwen Brønsted and Lewis acidity, it can relate site strength to the nature of the sites present (33, 34). In zeolites, the strong sites (>160 kJ/mol) observed at low NH_3 coverage have been attributed to Lewis centers (33, 34) resulting from extraframework Al species produced during thermal and hydrothermal treatments. Sites of intermediate strength of adsorption (i.e., 130–160 kJ/mol) have been associated with Brønsted centers resulting mainly from bridging hydroxyls. Heat of adsorption in the range 100–130 kJ/mol represents weak Lewis sites and below 100 kJ/mol what is observed is the interaction of the probe molecule with weak silanol groups (33–35).

Microcalorimetry (36, 37) results with ammonia and pyridine as the probe molecules are reported in Tables 6 and 7 and in Figs. 8 and 9. Chemisorption isotherms are shown in Fig. 8. Not shown are secondary sorption isotherms, that is, sorption isotherms for samples after NH_3 or pyridine adsorption and degassing under vacuum at 150°C. By subtracting the adsorbed volume of the secondary isotherms from that of the primary isotherms at the same equilibrium pressure ($p = 0.2$ torr), it is possible to obtain V_{Irr}, the volume of irreversibly chemisorbed sorbate. This value is believed to correlate with the presence of strong acid sites (36, 37). In Tables 6 and 7, initial heats have been associated with the strength of the strongest acid sites present (36, 37). On the other hand, integral heats represent the total heat of adsorption evolved at $p = 0.2$ torr and are therefore associated with the solid's acid site density.

TABLE 6

Ammonia Chemisorption Data at 150°C ($p = 0.2$ torr)

					kJ/mol		
	In. H.	Int. H.	V_T	V_{Irr}	<100	100–150	>150
Fresh FCC	166	67.6	588	381	181	378	29
Steam-aged FCC	154	5.8	103	50	88	11	5
Equilibrium FCC	166	6.2	95	47	84	6	6
Regenerated FCC	170	10.2	110	54	69	30	11

Note. Initial heats (In. H.) are in kJ/mol. Integral heats (Int. H) are in J/g. V_T, V_{Irr}, and the population of sites with a given strength are in μmol NH_3/g.

TABLE 7

Pyridine Chemisorption Data at 150°C ($p = 0.2$ torr)

					kJ/mol		
	In. H.	Int. H.	V_T	V_{Irr}	100–150	150–200	>200
Fresh FCC	249	57.8	442	301	35	59	132
Steam-aged FCC	201	9.7	126	83	15	12	10
Equilibrium FCC	249	8.5	110	71	8	7	15
Regenerated FCC	245	8.9	105	57	7	9	17

Note. Initial heats (In. H.) are in kJ/mol. Integral heats (Int. H) are in J/g. V_T, V_{Irr}, and the population of sites with a given strength are in μmol pyridine/g.

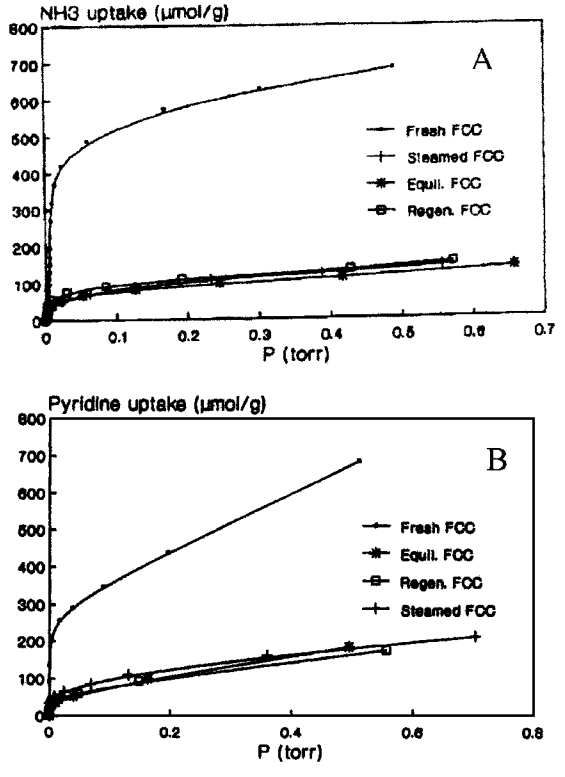

FIG. 8. Sorption isotherms for fresh, steam-aged, equilibrium, and regenerated FCCs. (A) Ammonia and (B) pyridine.

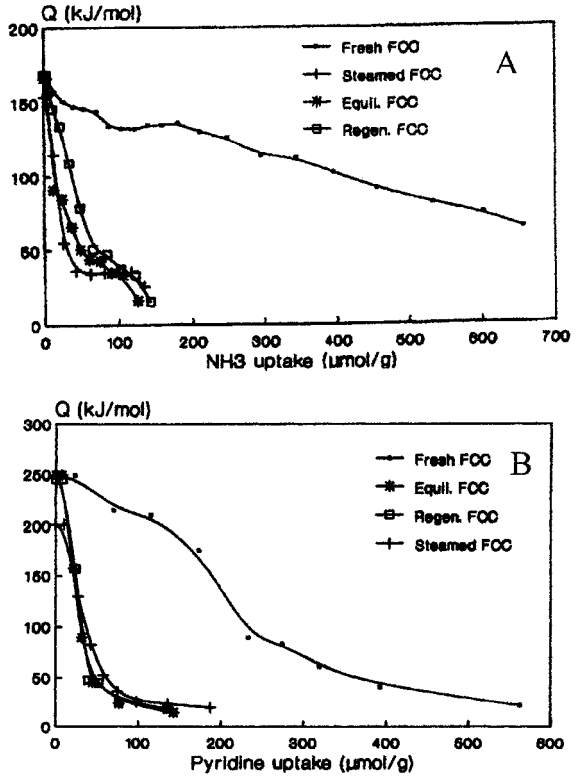

FIG. 9. Differential heat profiles for fresh, steam-aged, equilibrium, and regenerated FCCs. (A) Ammonia and (B) pyridine.

The differences in NH_3 and pyridine sorption shown in Fig. 8 and in Tables 6 and 7 reflect the loss of surface area and crystallinity that a fresh FCC experiences after aging. Similar results have been obtained while studying a FCC sample having different composition (23). Although after aging, integral heats of NH_3 chemisorption decrease drastically, initial heats in the fresh and equilibrium FCC remain essentially unchanged and increase in the regenerated FCC; see Table 6. Differences in initial heat values between the steam-aged and equilibrium FCCs could be due in part to the different porosities of the two catalysts; see Table 3. In addition, NH_3 interactions with metal (Ni, V, Fe) impurities may have contributed to initial heats measured in the equilibrium FCC.

Interestingly, the DEMET process increases both integral and initial heats and the strength of the strongest acid sites increases above that measured in the fresh FCC; see Table 6. The various acid treatments used during metal removal have further dealuminated the catalyst components and produced additional acid sites responsible (in part) for the enhanced acidity observed; see Table 6.

Similar results have also been obtained with pyridine; see Table 7. When using pyridine, initial heats in the fresh and used FCCs remain constant, near 245–249 kJ/mol, while integral heat, V_T, and V_{irr} decrease drastically because of losses of acid site density; see Table 7. A larger probe molecule such as pyridine enhances the difference in initial heat values between the steam-aged and the mesopores containing an equilibrium FCC sample; see Tables 6 and 7. However, in contrast to ammonia, pyridine chemisorption does not provide significant differences between the acidity of equilibrium and regenerated FCCs, indicating that the new acid sites originated by the DEMET process are preferentially located in the small micropores present in the regenerated FCC.

The corresponding differential heats of ammonia and pyridine adsorption as a function of coverage are shown in Fig. 9. When using ammonia, in addition to some strong Lewis sites with strength near 170 kJ/mol, the fresh FCC contains two populations of sites; see Fig. 9A. The smaller population of sites with strength near 145 kJ/mol is attributed to the FCC acidic component, which in this case is an HY-type zeolite (20–30 wt%) stabilized by a low level of RE cations; see Table 1. The larger population of sites with strength near 134 kJ/mol has been attributed to the FCC matrix, which in this case is probably an aluminosilicate similar to AAA-alumina (20). As observed in other FCCs (33, 36, 37), after steam-aging there is a sharp decrease in the FCC acidity that can be safely attributed to losses of Si(OH)Al groups in the zeolites and in the aluminosilicate matrix. Aging induces a drastic loss in acid site density, leaving a porous structure containing a heterogeneous distribution of site strength; the strength of these sites monotonically decreases with NH_3 coverage; see Table 6 and Fig. 9A. Initial heats as well as acid site density in the regenerated FCC are greater than in the steam-aged and equilibrium samples; see Fig. 9A.

The differential heat profiles for pyridine shown in Fig. 9B are in qualitative agreement with those in Fig. 9A for ammonia. Initially, in the fresh FCC, there is a small population of sites with strength near 249 kJ/mol followed by a larger population ($\sim$100 μmol pyridine/g) with strength near 210 kJ/mol and by a minor population with strength near 80 kJ/mol representing the interaction of pyridine with weak silanol groups. In Fig. 9B, the more energetic sites have been attributed to the interaction of pyridine with non-framework Al species and with Si(OH)Al sites, respectively (33–35). Similar to what is observed with ammonia, aging in a FCCU has negligible effects on initial heats, that is, on the strength of the strongest sites in the used FCC samples. Then as pyridine coverage increases, acid site strength monotonically decreases and curves for the the catalysts under study overlap each other; see Fig. 9B. These results are consistent with those obtained when using pyridine as the probe molecule to investigate the acidity of clay- based FCCs (32) and of other commercial FCC samples (23).

Atomic Force Microscopy

With hard surfaces such as clays (38), image generation by scanning probe microscopy is dominated by the surface

topology, by the tip geometry, and, when working in air, by the meniscus force of a water film on the surface. This force and the large contact area between the tip and the surface are the main sources of image artifacts when studying hard surfaces. It is believed that by rotating the image, changing scan speed, and varying the imaging force, it is possible to distinguish between artifacts and real topographical features of FCC surfaces (38). Moreover, by using AFM images in conjunction with digitally stored line profiles, the AFM software allows the quantitative determination of pore diameters and pore size distributions. The simultaneous use of images and profiles greatly facilitates the identification of pores as well as the architecture that surrounds the pore's entrance.

The large-scale images in Fig. 10 closely resemble those obtained for other fresh FCCs (15, 39). That is, the surface topography appears to be dominated by a densely packed but disordered array of particles irregular in size or shape; see Figs. 10A and 10B. These particles are mainly aggregates of platelets and their mode of aggregation can form large openings on the FCC surface responsible for the catalyst porosity; see Fig. 10C. In Fig. 10C, the deep cavity on the FCC surface is about 0.5 μm in width and over 3 μm in length. These large surface openings could occlude and retain high-molecular-weight hydrocarbons that cannot be removed during steam-stripping, thus contributing to the FCC overall coke generation (39). The large pores shown in Fig. 10C appear whenever stacks of clay platelets are found near the FCC surface (15, 39). These clay particle aggregates can create large valleys or cracks that could decrease the FCC microspheres' attrition resistance. As observed previously (15, 39), elongated slits with width (w) in the range 5–15 nm and length (l) such that $l/w \ggg 1$ appear to be the main source of the FCC surface porosity; see Fig. 10D.

Many of the surface characteristics observed for the fresh FCC can be seen also in the corresponding equilibrium

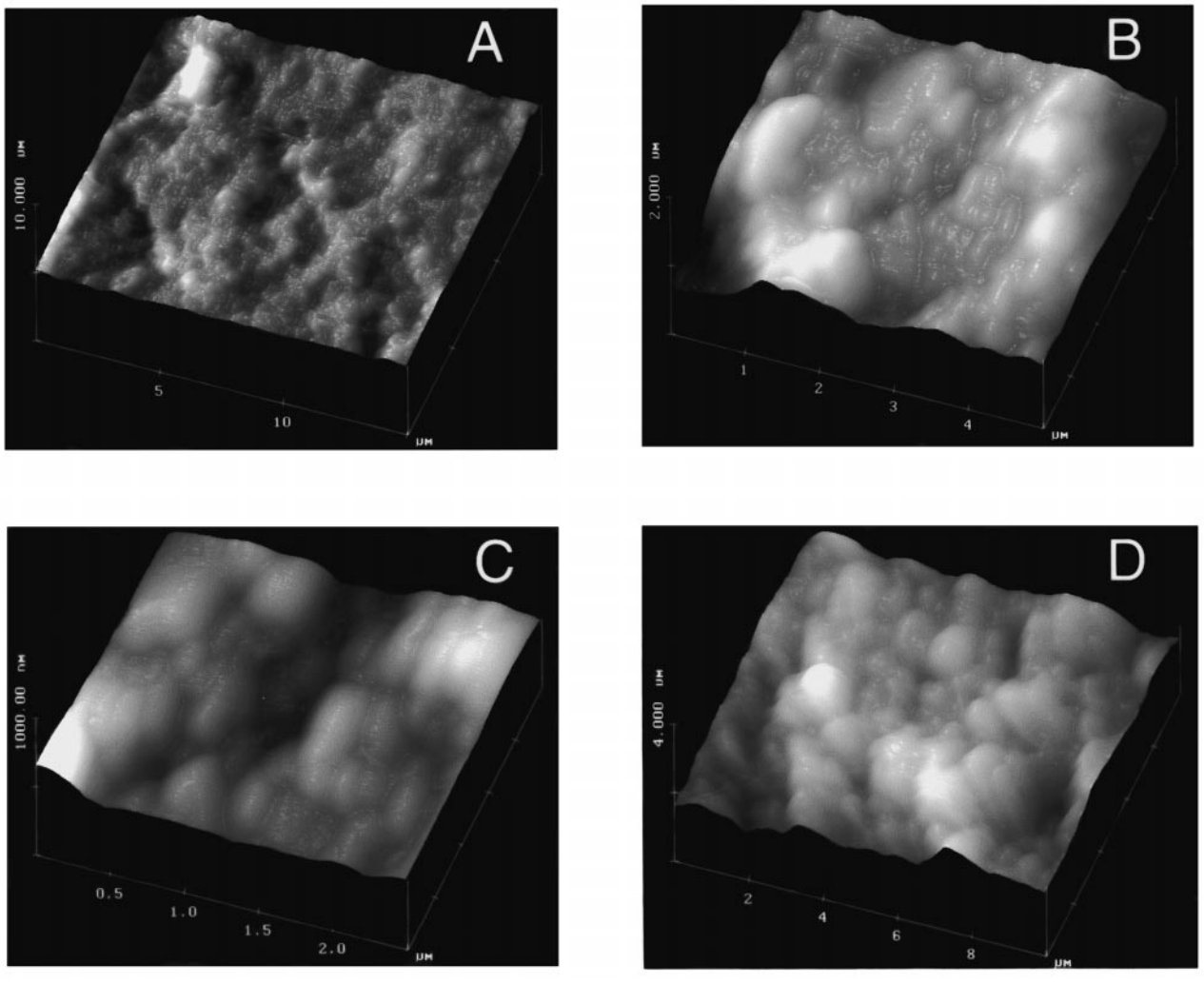

FIG. 10. Contact-mode AFM images in air of the fresh FCC showing (A) top view of the FCC surface, (B) top view of plates showing agglomeration, (C) top view image showing the elongated cracks that form the surface micropores, and (D) particles agglomeration and surface porosity.

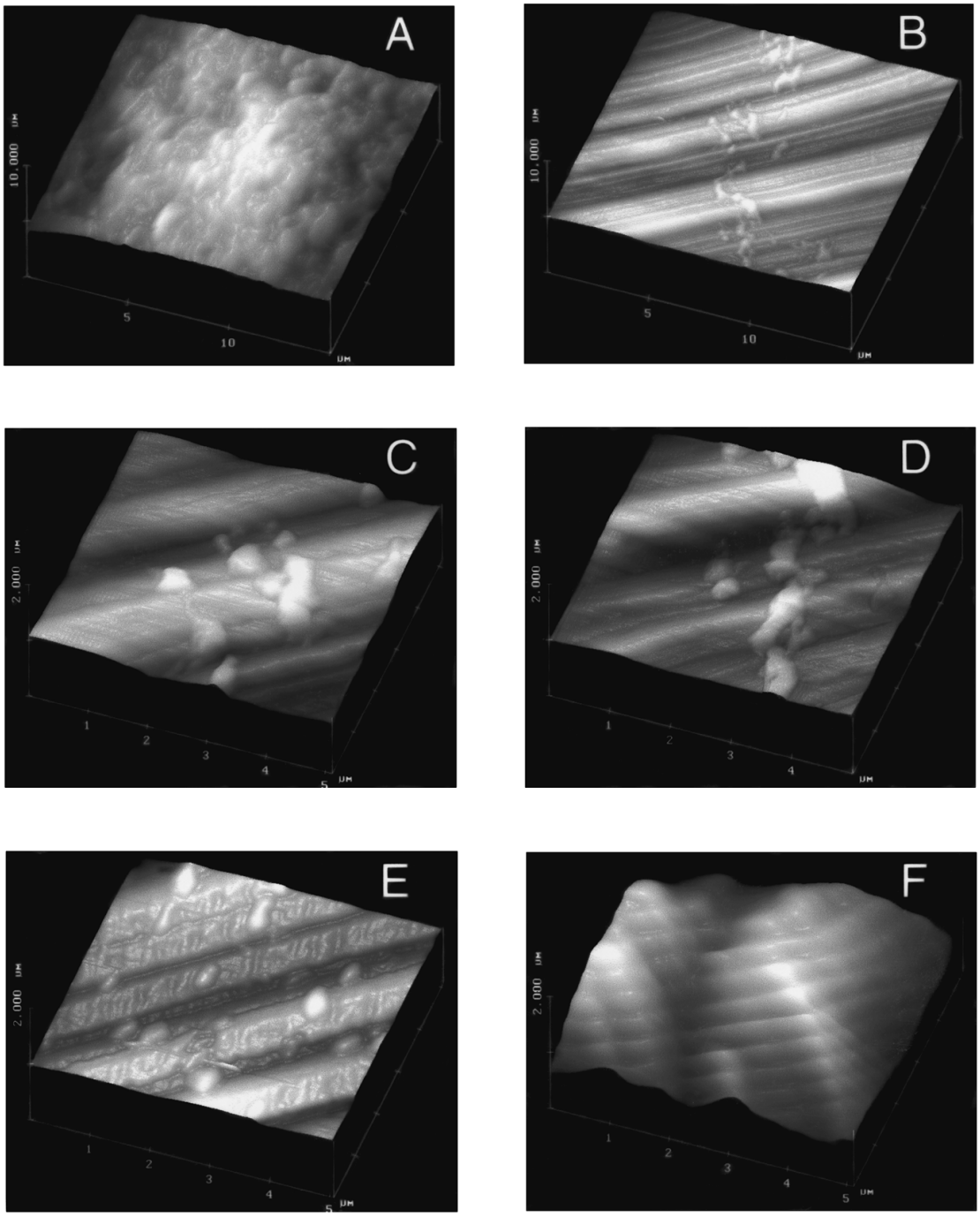

FIG. 11. Contact-mode AFM images in air of the equilibrium FCC showing (A) granular aspect of the surface, (B) plate aggregates and the deposition of surface debris, (C) surface cracks and debris deposition, (D) ribbon-like fragments of debris between plates and cracks, (E) surface debris granular in shape, and (F) debris-free stacks of clay platelets and typical surface cracks.

sample. However, the roughness of the surface appears to have decreased as in Fig. 11A and surface debris oftentimes can be observed on the stacks of plates (probably kaolin) that form the catalyst surface; see Fig. 11B. Although the AFM can describe the FCC surface with unprecedented resolution, it cannot provide information concerning its chemical composition. Thus the exact nature of the debris in Figs. 11B–11E remains unknown. It can be speculated that, since vanadia melts during the regeneration cycle, the fragmented ribbon-like particles in Figs. 11C and 11D represent V_2O_5 impurities, whereas the granular debris in Fig. 11E represents the more refractory NiO deposits. Figure 11F

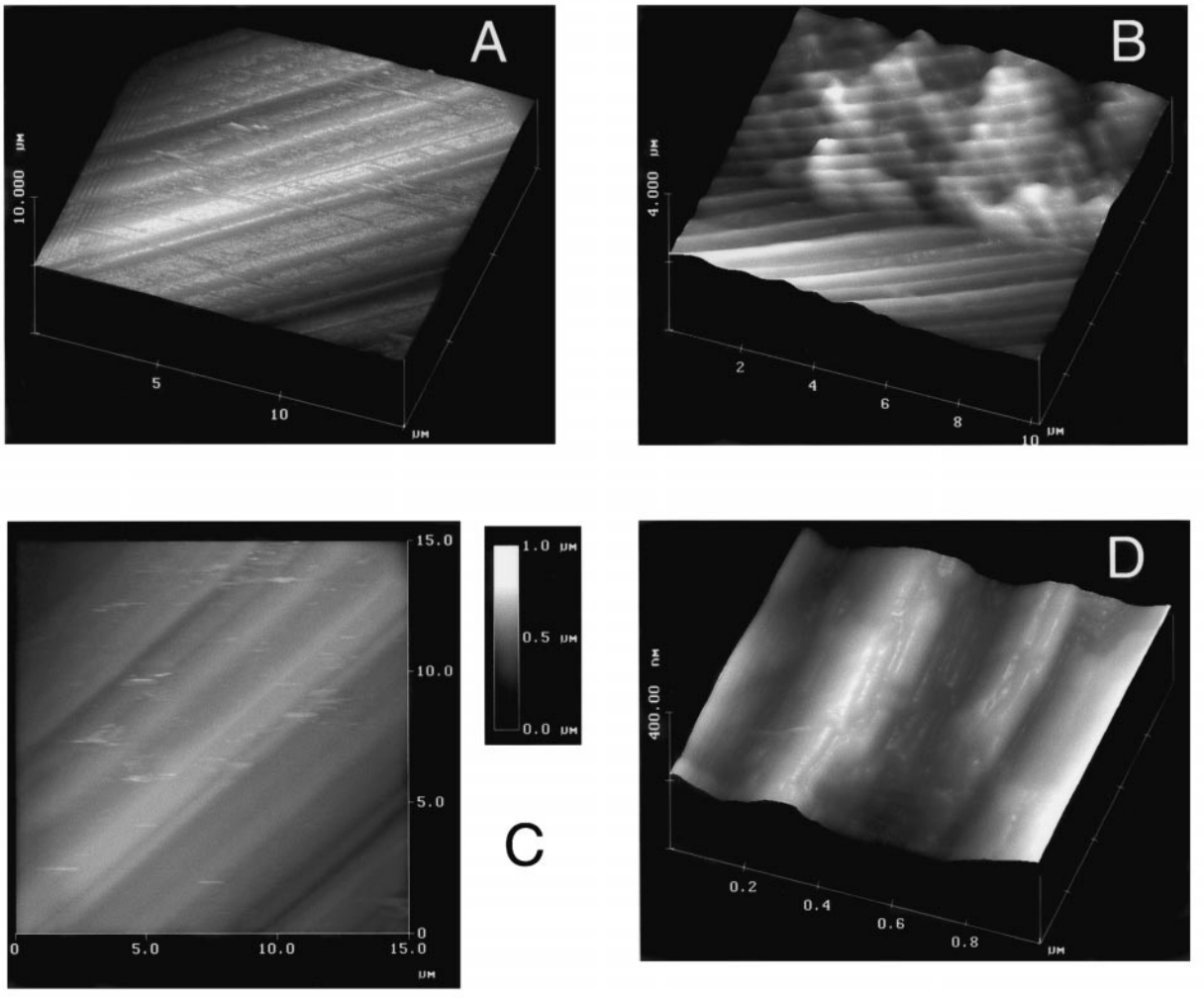

FIG. 12. Large-scale contact-mode side-view AFM images in air of the regenerated FCC showing (A) typical surface topography, (B) particle agglomeration and formation of surface porosity, (C) reduced surface roughness, and (D) large plates free from surface deposits.

shows a 5×5-μm region of the equilibrium FCC that is free of surface debris.

The large-scale ($10\,\mu\text{m} \times 10\,\mu\text{m}$) image in Fig. 12A is typical of the regenerated FCC. The surface roughness appears diminished and debris is no longer visible on the surface in Fig. 12A or between the clay platelets that oftentimes form the catalyst surface; see Fig. 12B. After regeneration, the FCC NiO and V_2O_5 content decreases from 0.99 and 0.60% to 0.19 and 0.03%, respectively. The small amount of surface debris in Fig. 12C may represent residual metal impurities. However, the images in Fig. 11D together with those in Figs. 12A and 12B best describe the surface of the regenerated FCC sample.

Microactivity Test Results

Results in Table 8 show the anticipated difference in activity between steam-aged and metal-containing equilibrium FCC samples (23). When a fresh FCC is deactivated under MAT conditions, all the microspheres experience the same time exposure to steam and temperature in a metal-free environment. By contrast, an equilibrium FCC sample is composed of microspheres that, in addition to exposure to metal contaminants, have experienced different residence times in the FCCU and therefore have been deactivated to a different extent (9, 10). The accelerated aging procedures used to deactivate fresh FCCs under MAT conditions are nonetheless useful for ranking the merits of experimental FCCs and for choosing catalysts that deserve further investigation and pilot plant testing.

The most interesting aspect of the MAT results in Table 8 is the indication that the DEMET regeneration procedure can restore in a spent FCC an activity that surpasses that of the equilibrium catalyst in operation in the FCCU from which the sample was obtained. The greater activity allows the regenerated FCC to crack more of the gas oil

TABLE 8

Microactivity Test Results for Steam-Aged, Equilibrium, and Regenerated FCCs

	Steam-aged FCC	Equil. FCC	Regen. FCC
Conversion (wt% ff)	75.1	66.4	69.7
Gasoline (wt% ff)	48.5	45.0	46.4
LCGO (wt% ff)	13.3	16.2	14.5
SO (wt% ff)	11.6	17.5	15.8
Carbon (wt% ff)	3.5	5.5	3.5
Hydrogen (wt% ff)	0.06	0.50	0.14
Hydrogen sulfide (wt% ff)	1.70	1.70	1.70
Methane (wt% ff)	0.98	0.76	0.71
Ethane (wt% ff)	0.73	0.49	0.47
Ethylene (wt% ff)	0.94	0.55	0.69
Dry gas (wt% ff)	4.4	4.0	3.7
Propane (wt% ff)	1.65	0.79	1.0
Propylene (wt% ff)	5.0	3.5	4.7
n-Butane (wt% ff)	1.3	0.58	0.79
Isobutane (wt% ff)	4.6	2.1	3.2
1-Butene (wt% ff)	1.4	1.1	1.4
Isobutylene (wt% ff)	1.6	1.5	2.0
cis-2-Butene (wt% ff)	1.3	1.0	1.3
trans-2-Butene (wt% ff)	1.7	1.3	1.6
Butadiene (wt% ff)	0.06	0.03	0.03
C_4-olefins	6.1	4.9	6.3

Note. A reactor temperature of 540°C and a C/O = 3.0 were used. Material balance ~99%.

heavy components, thus decreasing the remaining slurry oil ($343C^+$) while producing more gasoline without increasing coke generation (Table 8); the gasoline/conversion ratio remains in the 0.67 to 0.68 range. The regenerated and equilibrium FCCs have a coke/conversion ratio of 0.050 and 0.083, respectively. Moreover, the regenerated FCC yields less dry gas and more low-molecular-weight olefins; the $C_3^{2=}/\Sigma C_3$ and the $C_4^{2=}/\Sigma C_4$ ratios remain near 0.8 and 0.6, respectively, indicating that the H transfer properties of the catalysts did not change significantly during regeneration.

It has been postulated that the main cracking reaction during gas oil conversion is the β-scission of a carbonium ion to form an olefin and a new, lower molecular weight carbonium ion (40). Microcalorimetry results presented in this paper have revealed the absence in equilibrium FCCs of strong proton donor sites that could protonate a paraffin to form carbonium ions. In fact, NMR spectra have shown that the cracking component in the aged FCCs in Table 8 is essentially de-aluminated and that the Al lost by the faujasite framework forms extraframework Al(IV), Al(V), and Al(VI) species. Acid site density from microcalorimetry is drastically reduced and only a few strong L- type sites are present. These results are more consistent with a gas oil cracking mechanism that is initiated by hydride abstraction by strong L-sites such as Al(V) species. Carbenium ions thus formed could undergo cracking (β-scission) to produce a smaller paraffin and another carbenium ion that will propagate the cracking reactions responsible for gas oil conversion. The role of carbenium ions and of the catalytic cracking of paraffins has been described in detail elsewhere (41).

SUMMARY AND CONCLUSIONS

In a typical commercial FCCU, steam stripping of occluded hydrocarbons from the FCC surface is performed at temperatures in the range 480–540°C. Higher temperatures (600–700°C) are seen by the FCC in the regenerator where, however, steam rarely exceeds the 20% limit. The severity of the hydrothermal treatment, like that described in this paper and in the literature, is necessary to reduce the structural and catalytic properties of experimental FCCs near equilibrium levels in a short (~5–10 h) period of time. Since different FCCs may deactivate differently, a variety of deactivation conditions and procedures are needed to predict the activity of each FCC available to refiners.

The steam-aging procedure used in this study (5 h with 100% steam at 760°C and 1 atm) approximates only in part the aging process that the type of FCC examined experiences in a refinery's FCCU. In fact, PSD data indicate that aging increases the equilibrium FCC mesoporosity at the expense of its microporosity and crystallinity. The formation of mesopores with APD = 5.5 nm was not observed in the steam-aged FCC under MAT conditions.

The ^{29}Si NMR spectrum of the parent FCC can be considered as a superposition of spectra from an HY-type zeolite, kaolin, and an aluminosililicate gel, its three main components. Interestingly, in the steam-aged and equilibrium FCCs, the typical five-peak pattern of HY zeolites disappears and is replaced by a single sharp resonance near −107 ppm, indicating that the FCC active component (i.e., the HY-type zeolite) has undergone drastic dealumination, producing faujasite crystals containing only minimal amounts of T[(4-*n*)Si, *n*Al] sites. The ^{29}Si NMR spectra of the steam-aged and equilibrium FCCs are almost indistinguishable from one another, thus showing that the accelerated aging procedure used reduces the structural properties of the acidic component to those produced, over a period of several weeks, in a refinery FCCU. In contrast, the corresponding ^{27}Al MAS NMR spectra have indicated that the distributions of coordination environments of extraframework Al present in the steam-aged and equilibrium FCC samples are somewhat different. In fact, the steam-aged sample contains comparable amounts of Al(IV), Al(V), and Al(VI) species, whereas in the equilibrium and regenerated FCCs lesser amounts of Al(V) are present and Al(VI)/Al(IV) $\gg$ 1. The effects of different Al(IV), Al(V), and Al(VI) distributions on the cracking properties of FCCs remain to be investigated.

In agreement with ^{29}Si NMR, microcalorimetry experiments with NH_3 and pyridine have shown that after aging,

the parent FCC loses most of its population of acid sites. In fact, although the strength of the strongest sites (Lewis sites) does not change significantly there is a drastic decrease in acid site density. Evidence of chemisorption on Si-OH-Al linkages cannot be observed in FCCs aged under MAT conditions or in a FCCU, owing to losses of framework Al from the zeolite and from the aluminosilicate matrix that bind together the FCC components. The presence of extraframework Al in mesopores formed after aging HY crystallites has been observed by HREM (9, 10).

AFM images of the surface of the fresh, equilibrium, and regenerated FCCs show similar surface topographies. The main distinguishing feature of the equilibrium FCC surface is the presence of regions containing surface debris that is no longer easily visible after regeneration. Elemental analysis data have indicated that in regenerated FCCs, metal (Ni, V, Fe) contaminants are drastically reduced. Thus the surface impurities observed in AFM images are likely to represent nickel and vanadium compounds deposited during gas oil cracking.

The DEMET process of FCC regeneration removes metal contaminants without affecting the equilibrium FCC porous structure. Moreover, ^{29}Si NMR spectra indicate that the HY zeolite in the regenerated catalyst no longer show evidence of framework Al. Thus even if framework Al is no longer observable in the HY component by NMR, the FCC can retain its cracking activity. The gain in cracking activity exhibited by the spent FCC after DEMET regeneration is attributed to an increase in its L-type acidity and to metal removal from the FCC surface and porous structure. When this occurs, previously unused microporosity becomes available to hydrocarbon sorption and catalytic cracking.

In summary, ^{29}Si and ^{27}Al MAS NMR, together with microcalorimetry and MAT results, indicates that FCCs that contain de-aluminated faujasite crystals can exhibit high cracking activity during gas oil conversion. Acid site density plays a minor role in FCC activity and as long as the strength of the strongest acid sites (L-type sites) is retained and as long as these sites are available to gas oil, the FCC will maintain its useful cracking activity. These results lend support to the possibility that gas oil cracking is initiated by hydride abstraction on strong L-sites with formation and cracking of carbenium ions. Although steam-aging of newly prepared FCCs under MAT conditions is only partially successful in reducing the properties of the catalyst to those observed in equilibrium samples, it remains a valuable screening test to quickly identify those experimental FCCs that merit further study or pilot plant evaluation.

ACKNOWLEDGMENTS

This work has been supported in part by NATO Collaborative Grant CRG-971497 to M.L.O. and H.E. and, initially, by an unrestricted grant from Coastal to G.T.R.I. Special thanks are due to A. E. Schweizer (Exxon) for elemental analysis, to J. Gonzales (Akzo Nobel) for MAT data, and to S. Pavel for useful discussions and initial support.

REFERENCES

1. MacCoy, M., *Chem. Eng. News*, Sept. 20, 17 (1999).
2. Pavel, S. K., *in* "Fluid Cracking Catalysts" (M. L. Occelli and P. O'Connor, Eds.), p. 291. Dekker, New York, 1997.
3. Habib, T. H., and Venuto, P. B., "Fluid Catalytic Cracking with Zeolite Catalysts," Dekker, New York, 1979.
4. Burk, E. H., Erickson, H., and Anderson, A. D., U.S. Patent 3,122,510 (1978).
5. Occelli, M. L., Kowalczyk, D. C., and Kibby, C. L., *Appl. Catal.* **16**, 227 (1985).
6. Mauge, F., Courcelle, J. C., Engelhard, Ph., Gallezot, P., and Grosmangin, J., *in* "New Developments in Zeolite Science and Technology" (Y. Muricami *et al.*, Eds.), p. 804. Elsevier, Amsterdam, 1986.
7. Gallezot, P., Feron, B., Bourgogne, M., and Engelhard, Ph., *in* "Zeolites: Facts, Figures, Future" (P. A. Jacob *et al.*, Eds.), p. 1281. Elsevier, Amsterdam, 1989.
8. Gelin, P., and Des Courieres, T., *Appl. Catal.* **72**, 179 (1991).
9. Beyerlein, R. A., Tamborski, G. A., Marshall, C. L., Meyers, B. L., Hall, J. B., and Huggins, B. J., *in* "Fluid Catalytic Cracking II: Concepts in Catalysts Design" (M. L. Occelli and P.O'Connor, Eds.), p. 109. Am. Chem. Soc., Washington, DC, 1991.
10. Beyerlein, R. A., Choi-Feng, C., Hall, J. B., Huggins, B. J., and Ray, G. J., *in* "Fluid Catalytic Cracking III: Materials and Processes" (M. L. Occelli and P.O'Connor, Eds.), p. 81. Am. Chem. Soc., Washington, DC, 1994.
11. Musselman, I. H., Russel, P. E., Chang, R. T., Jamieson, M. G., and Sawyer, L. C., *in* "Proceedings, 12th International Congress on Electron Microscopy, Seattle, August, 1990" (W. Bailey, Ed.), p. 866. San Francisco Press, San Francisco, 1990.
12. Binnig, J., Rohrer, H., Gerber, C., and Weibel, E., *Phys. Rev. Lett.* **50**, 120 (1983).
13. Albrecht, T. R., Dovek, M. M., Lang, C. A., Grutter, P., Quate, C. F., Kuan, S. N. J., Frank, C. W., and Pease, R. F. W., *J. Appl. Phys.* **64**, 1178 (1988).
14. Occelli, M. L., Gould, S., and Drake, B., *in* "Fluid Catalytic Cracking III: Materials and Processes" (M. L. Occelli and P. O'Connor, Eds.), ACS Symposium Series, Vol. 571, p. 20. Am. Chem. Soc., Washington, DC, 1994.
15. Brunauer, S., Emmett, P. H., and Teller, E., *J. Am. Chem. Soc.* **60**, 309 (1938).
16. Seaton, N. A., Walton, J. R., and Quirke, N., *Carbons* **27**, 853 (1994).
17. Webb, P. A., Olivier, J. P., and Conklin, W. B., *Am. Lab.* 38 (1994).
18. Olivier, J. P., *J. Porous Mater.* **3**, 9 (1995).
19. Olivier, J. P., Koch, S., Jaroniec, M., and Kruk, M., *in* "Characterization of Porous Solids V" (K. K. Unger *et al.*, Eds.), Studies in Surface Science and Catalysis, Vol. 128, p. 1. Elsevier, Amsterdam, 2000.
20. Occelli, M. L., Biz, S., Auroux, A., and Iyer, P. S., *Appl. Catal.* **179**, 117 (1999).
21. Scherzer, J., "Octane-Enhancing Zeolite FCC: Scientific and Technical Aspects." Dekker, New York, 1990.
22. Gregg, S. J., and Sing, K. S. W., "Adsorption, Surface Area and Porosity," 2nd ed. Academic Press, New York, 1982.
23. Occelli, M. L., Auroux, A., Baldiraghi, F., Leoncini, S., *in* "Fluid Cracking Catalysts" (M. L.Occelli and P. O'Connor, Eds.), p. 203. Dekker, New York, 1998.
24. Engelhard, G., and Michel, G., "High Resolution Solid State NMR of Silicates and Zeolites," Wiley, Chicester, 1987.
25. Grim, R. E., "Clay Minerology." McGraw-Hill, New York, 1968.

26. Occelli, M. L., *in* "Catalysts in Petroleum Refining and Petrochemical Industries" (M. Absi-Halabi *et al.*, Eds.), Studies in Surface Science and Catalysis, Vol. 100, p. 27. Elsevier, Amsterdam, 1995.
27. Gilson, J. P., Edwards, G. C., Peters, A. K., Rajagopalan, K., Wormsbecher, R., Roberie, T. G., and Shatlock, M. P., *J. Chem. Soc. Chem. Commun.* **1987**, 91 (1987).
28. Samoson, A., Lippmaa, E., Engelhardt, G., Lohse, D., and Jerschwitz, H. G., *Chem. Phys. Lett.* **134**, 589 (1987).
29. Samoson, A., Lippmaa, E., and Pines, A., *Mol. Phys.* **65**, 1013 (1988).
30. Ray, G. J., and Samoson, A., *Zeolites* **13**, 410 (1993).
31. Hong, H., Coster, D., Chen, F. R., Davis, J. G., and Fripiat, J. J., "New Frontiers in Catalysis" (L. Guczi, Ed.), p. 1159. Elsevier, Amsterdam, 1993.
32. Chen, D., Sharma, S., Cardona-Martinez, N., Dumesic, J. A., Bell, V. A., Hodge, G. D., and Madon, R. J., *J. Catal.* **136**, 392 (1992).
33. Auroux, A., and Ben Taarit, Y., *Therm. Acta* **122**, 63 (1987).
34. Shi, Z. C., Auroux, A., and Ben Taarit, Y., *Can. J. Chem.* **66**, 1013 (1983).
35. Cardona-Martinez, N., and Dumesic, J. A., *J. Catal.* **125**, 427 (1990).
36. Auroux, A., "Catalyst Characterization: Physical Techniques for Solid Materials" (B. Imelik and J. C. Vedrine, Eds.), Chap. 22. Plenum, New York, 1994.
37. Auroux, A., *Top. Catal.* **4**, 71 (1997).
38. Wicks, F. J., Henderson, G. S., and Vrdolijak, G. A., *in* "Scanning Probe Microscopy of Clay Minerals" (K. L. Nagy and A. E. Blum, Eds.), CMS Workshop Lectures, Vol. 7, p. 92. 1994.
39. Occelli, M. L., Gould, S. A. C., Baldiraghi, F., Leoncini, S., *in* "Fluid Cracking Catalysts" (M. L. Occelli and P. O'Connor, Eds.), p. 227. Dekker, New York, 1998.
40. Venuto, P. B., and Habib, E. T., "Fluid Catalytic Cracking with Zeolites." Dekker, New York, 1979.
41. Cortright, R. D., Dumesic, J. A., and Madon, R. J., *Top. Catal.* **4**, 15 (1997).